


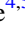




Black Hole–Black Hole Total Merger Mass and the Origin of LIGO/Virgo Sources

Krzysztof Belczynski¹, Zoheyr Doctor² , Michael Zevin^{3,4} , Aleksandra Olejak¹ , Sambaran Banerjee^{4,5} , and Debatri Chattopadhyay⁶

¹ Nicolaus Copernicus Astronomical Center, Polish Academy of Sciences, Bartycka 18, 00-716 Warsaw, Poland; chrisbelczynski@gmail.com, aleksandra.olejak@wp.pl

² Center for Interdisciplinary Exploration and Research in Astrophysics (CIERA) and Department of Physics & Astronomy, Northwestern University, 1800 Sherman Ave, Evanston, IL 60201, USA; zoheyr.doctor@gmail.com

³ Kavli Institute for Cosmological Physics, The University of Chicago, 5640 South Ellis Avenue, Chicago, IL 60637, USA; michael.j.zevin@gmail.com

⁴ Enrico Fermi Institute, The University of Chicago, 933 East 56th Street, Chicago, IL 60637, USA

⁵ Helmholtz-Institut für Strahlen- und Kernphysik (HISKP), Nussallee 14-16, D-53115 Bonn, Germany; sambaran.banerjee@gmail.com

⁶ Argelander-Institut für Astronomie (AIfA), Auf dem Hügel 71, D-53121 Bonn, Germany; chattopadhyaydebatri@gmail.com

⁷ Gravity Exploration Institute, School of Physics and Astronomy, Cardiff University, Cardiff, CF24 3AA, UK

Received 2022 April 25; revised 2022 June 19; accepted 2022 July 13; published 2022 August 23

Abstract

The LIGO–Virgo–KAGRA (LVK) Collaboration has reported nearly 100 black hole (BH)–BH mergers. LVK provides estimates of rates, masses, effective spins, and redshifts for these mergers. Yet the formation channel(s) of the mergers remains uncertain. One way to search for a formation site is to contrast the properties of detected BH–BH mergers with different models of BH–BH merger formation. Our study is designed to investigate the usefulness of the total BH–BH merger mass and its evolution with redshift in establishing the origin of gravitational-wave sources. We find that the average *intrinsic* BH–BH total merger mass shows exceptionally different behaviors for the models that we adopt for our analysis. In the local universe ($z = 0$), the average merger mass changes from $\bar{M}_{\text{tot,int}} \sim 25 M_{\odot}$ for the common envelope binary evolution and open cluster formation channels, to $\bar{M}_{\text{tot,int}} \sim 30 M_{\odot}$ for the stable Roche lobe overflow binary channel, to $\bar{M}_{\text{tot,int}} \sim 45 M_{\odot}$ for the globular cluster channel. These differences are even more pronounced at larger redshifts. However, these differences are diminished when considering the LVK O3 detector sensitivity. A comparison with the LVK O3 data shows that none of our adopted models can match the data, despite the large errors on BH–BH masses and redshifts. We emphasize that our conclusions are derived from a small set of six models that are subject to numerous known uncertainties. We also note that BH–BH mergers may originate from a mix of several channels, and that other (than those adopted here) BH–BH formation channels may exist.

Unified Astronomy Thesaurus concepts: [Black hole physics \(159\)](#)

1. Introduction

The latest LIGO–Virgo–KAGRA (LVK) Collaboration catalog, GWTC-3 (The LIGO Scientific Collaboration 2021a), reports the detection of 90 double compact object mergers, 83 of which are confidently classified as binary black hole (BH) mergers. The LVK Collaboration also provided estimates of the intrinsic population properties of these mergers, such as their distributions of rates, masses, and effective spins. The merger rate density of BH–BH systems at a fiducial redshift of $z = 0.2$ is $17.3\text{--}45 \text{ Gpc}^{-3} \text{ yr}^{-1}$, and the rate increases with redshift (The LIGO Scientific Collaboration 2021c). The masses of BH–BH mergers show complex multifeature behavior (Tiwari & Fairhurst 2021; The LIGO Scientific Collaboration 2021c; Edelman et al. 2022). BH–BH merger effective spins are mostly positive and small ($0 < \chi_{\text{eff}} < 0.3$), with a $\sim 10\%$ – 30% contribution of mergers with high positive ($\chi_{\text{eff}} > 0.3$) effective spins (Abbott et al. 2021a, 2021b; Roulet et al. 2021).

Despite all the available information and the rapidly increasing number of detected BH–BH mergers, their origin and specific formation mechanism is not known. Several formation channels are under close investigation, each corresponding to a specific formation site of BH–BH mergers

and the specific evolutionary processes involved in the evolution of BH–BH progenitors. The evolution of binary systems in isolation (galactic fields) can provide ample resources for BH–BH merger formation via several subchannels: evolution that involves a common envelope (CE) phase (e.g., Belczynski et al. 2016a; Giacobbo & Mapelli 2018; Kinugawa et al. 2021; García et al. 2021), evolution that only requires binary interactions through stable Roche lobe overflow (RLOF; e.g., van den Heuvel et al. 2017; Neijssel et al. 2019; Bavera et al. 2021; Olejak et al. 2021), and chemically homogeneous evolution, which requires rapidly rotating stars (e.g., de Mink & Mandel 2016; Mandel & de Mink 2016; Marchant et al. 2016). The evolution of objects in dense stellar systems may also provide satisfactory conditions for the dynamical formation of BH–BH mergers: in young open clusters (OCs; e.g., Banerjee 2018a; Di Carlo et al. 2020; Kremer et al. 2020; Rastello et al. 2021; Chattopadhyay et al. 2022), in dense globular clusters (GCs; e.g., Rodriguez et al. 2016b; Askar et al. 2017; Antonini & Gieles 2020), and in massive nuclear clusters (e.g., Arca-Sedda & Capuzzo-Dolcetta 2017; Arca Sedda 2020; Fragione et al. 2022; Mapelli et al. 2021). There are also formation channels that bridge the two major classes above of isolated and dynamical BH–BH formation. Multiple systems, in particular triples and quadruples, are also estimated to produce BH–BH mergers through a combination of typical stellar evolution assisted by dynamical interactions of stars (e.g., Antonini et al. 2017; Safarzadeh et al. 2020). Alternatively,



Original content from this work may be used under the terms of the [Creative Commons Attribution 4.0 licence](#). Any further distribution of this work must maintain attribution to the author(s) and the title of the work, journal citation and DOI.

gas-assisted evolution in active galactic nucleus disks may provide a way of forming merging BH–BH systems (e.g., Samsing et al. 2020; Ford & McKernan 2021).

Identifying the actual BH–BH merger formation channel or channels is hindered by numerous modeling uncertainties (Arca Sedda & Benacquista 2019; Broekgaarden et al. 2022; Gallegos-Garcia et al. 2021; Belczynski et al. 2022). For example, merger rates for double compact objects vary by orders of magnitude for each formation channel (e.g., Mandel & Broekgaarden 2022), while predicted mass distributions are extremely sensitive to various model assumptions (e.g., Olejak et al. 2021). Ideally, a given model should fit all the physical properties (rates, masses, and spins) for all three double compact object types (BH–BH/BH–NS/NS–NS mergers; NS: neutron star). Before this is accomplished, we need to build an understanding of how the various model parameters change the properties of double compact objects within the various formation channels. Numerous studies have already been dedicated to merger rates, NS/BH spins, or compact object masses (e.g., Timmes et al. 1996; Lipunov et al. 1997; Belczynski et al. 2002; Podsiadlowski et al. 2003; Voss & Tauris 2003; Zampieri & Roberts 2009; O’Connor & Ott 2011; Dominik et al. 2012; Mapelli 2016; Arca Sedda et al. 2018; Spera et al. 2019; Stevenson et al. 2019; Broekgaarden et al. 2022; Ford & McKernan 2021; Olejak & Belczynski 2021; van Son et al. 2022). Many of the above studies present BH–BH merger masses, but the evolution of mass with redshift is usually not shown or discussed in detail. One notable exception is the work by van Son et al. (2022), who present detailed analyses of the primary (more massive) BH mass and its evolution with redshift for BH–BH mergers for two (RLOF and CE) subchannels of isolated binary evolution. No studies, however, have focused on the average total BH–BH mass and its evolution with redshift. Here, we present and discuss the cosmic evolution of the average total masses of BH–BH mergers arising from various evolutionary channels. We note that empirical studies have been performed to assess changes in the BH–BH mass distribution shape with redshift, but thus far no definitive evidence of such mass distribution evolution has been found (Fishbach et al. 2021; The LIGO Scientific Collaboration 2021c; Tiwari 2022).

2. Models of BH–BH Formation

2.1. Isolated Binary Evolution Models

We use three models of BH–BH formation from isolated binary stars that were calculated with the `StarTrack` population synthesis code (Belczynski et al. 2002, 2008). The standard evolution involves the evolution of massive binary stars with empirically derived initial conditions (Sana et al. 2012; de Mink & Belczynski 2015). In particular, for massive stars, the initial mass function (IMF) is adopted to be a power law ($\propto M^{-2.3}$), and it extends to an initial star mass of $150 M_{\odot}$. The input physics includes wind losses for massive stars: O/B star and Wolf–Rayet (WR)-type winds, in addition to luminous blue variable winds (Vink et al. 2001; Belczynski et al. 2010a). We treat the accretion onto compact objects during RLOF and from stellar winds using the approximations presented by King et al. (2001) and Mondal et al. (2020). CE evolution is treated with the energy balance prescription of Webbink (1984), and we limit the accretion onto compact objects during a CE phase to 5% of the Bondi rate (MacLeod et al. 2017). We employ two

models of core-collapse supernova (SN) engines in the NS/BH mass calculation (Fryer et al. 2012) that either allow (delayed SN engine) or do not allow (rapid SN engine) for filling in the lower-mass gap (the dearth of compact objects with mass $\sim 2\text{--}5 M_{\odot}$) with compact objects between NSs and BHs (Belczynski et al. 2012; Zevin et al. 2020). We assume a minimum BH mass of $2.5 M_{\odot}$. In fact, we use the updated variants of rapid and delayed SN engines from Olejak et al. (2022). This study allows for the gradual filling of the lower-mass gap with compact objects through a single parameter: f_{mix} . Isolated binary models employ either $f_{\text{mix}} = 0.5$ (close to the original delayed SN engine) and $f_{\text{mix}} = 4.0$ (close to the original rapid SN engine). For simplicity, when discussing binary models, we will refer to them as having delayed or rapid SN engine physics. Pulsational pair-instability SNe (PPSNe) and pair-instability SNe (PSNe) are assumed to be weak and allow for the formation of BHs with masses up to $\sim 55 M_{\odot}$ (Leung et al. 2019; Belczynski et al. 2020). We use the fallback-decreased NS/BH natal kicks, with $\sigma = 265 \text{ km s}^{-1}$ (Hobbs et al. 2005), and we do not allow CE survival for Hertzsprung gap donors (Belczynski et al. 2007). The results of the population synthesis calculations are postprocessed with the Madau & Fragos (2017) star formation rate history in the universe and with the evolving with redshift metallicity distribution for Population I/II stars, as presented in Belczynski et al. (2020), to allow the calculation of the BH–BH merger population for the redshift range $z = 0\text{--}15$.

The standard physics presented above produces a majority of BH–BH mergers through the classical (CE) isolated binary evolution channel. In this channel, binaries that undergo RLOF with a donor star that is approximately twice the mass of the accretor or more ($q \gtrsim 2$) are subject to CE evolution that leads to orbital decay, and may lead to BH–BH merger under favorable conditions. We adopt model M380.B from Olejak et al. (2021), which produces 99.5% of BH–BH mergers through CE evolution. The delayed SN engine is employed in this model.

In our second model, we adopt nonstandard CE development criteria, which allow for stable RLOF to proceed even for systems with donors as massive as eight times mass of the accretor ($q \lesssim 8$; Pavlovskii et al. 2017). Such evolution, also under favorable conditions, may lead to orbital decay and the formation of a BH–BH merger (van den Heuvel et al. 2017). We adopt model M480.B from Olejak et al. (2021), which produces 94% of BH–BH mergers through stable RLOF evolution (and the rest through CE). The delayed SN engine is employed in this model.

In our third model, we adopt standard CE development criteria, but extend the IMF to $200 M_{\odot}$ and allow for less restrictive PPSN/PSN limits on BH mass. It has been argued that it is possible that the upper BH mass gap is located in a different place on the BH mass spectrum or may not exist at all (Farmer et al. 2020; Costa et al. 2021; Farrell et al. 2021). We adopt a model presented by Belczynski (2020) that avoids PPSN mass loss for helium core masses up to $M_{\text{He}} < 90 M_{\odot}$, with stars above this mass threshold destroyed by PSNe. This allows for the formation of BHs with masses up to $90 M_{\odot}$ from low-metallicity stars. The delayed SN engine is employed in this model.

In our fourth model, we adopt exactly the same input physics as in the third model, but we employ the rapid SN engine instead.

This sequence of models, with specific choices of input physics, has been designed to show the dependence of the total BH–BH merger mass on some of the most important and most uncertain parts of stellar and binary physics employed in our isolated binary evolution models.

2.2. GC Dynamical Models

We use GC models from the BH–BH formation channel analysis of Zevin et al. (2021), which have data relevant to this work publicly available on Zenodo. These models originate from a grid of 96 N -body models of collisionless star clusters simulated using the Hénon-style cluster Monte Carlo code CMC (Hénon 1971, Hénon 1971, Joshi et al. 2000, Pattabiraman et al. 2013), as described in Rodriguez et al. (2019). The cluster birth times and cluster initial metallicity follow cosmological models for GC formation (El-Badry et al. 2019), as outlined in Rodriguez & Loeb (2018) and Rodriguez et al. (2018a). In particular, clusters with three metallicities are used: $Z = 0.005$, 0.001, and 0.0002. The initial binary fraction for stars born in these cluster models is set to 10%, and is independent of stellar mass; the true value for the binary fraction of stars born in GCs is observationally unconstrained.

Stars and binaries that are born in GCs are evolved with rapid evolutionary formulas (Hurley et al. 2000, 2002), with updated prescriptions for stellar winds, compact object masses, and SN natal kicks (see Rodriguez et al. 2016a, 2018b). The initial masses of single stars and primaries in binary systems are taken from a Kroupa IMF ($\propto M^{-1.3}$, in the range 0.08–0.5 M_{\odot} , and $\propto M^{-2.3}$, in the range 0.5–150 M_{\odot}), with the secondary components in binaries drawn from a uniform mass ratio distribution. The semimajor axes of the initial binaries are drawn flat in $\log(P(a)da \propto 1/a)$, between the point of stellar contact and the hard–soft boundary, where the orbital velocity of the binary equals the typical velocity of the particles in the cluster (for a typical velocity of 10 km s^{-1} , this translates to $\sim 1\text{--}5 \times 10^5 R_{\odot}$ for equal-mass binaries with component masses between 30 M_{\odot} and 150 M_{\odot}). Eccentricities are drawn from a thermal distribution ($p(e) de = 2e de$). Stellar winds for massive stars are adopted from Vink et al. (2001) during the main sequence, and from Vink & de Koter (2005) for naked helium stars, with the later evolutionary stages following Belczynski et al. (2010a). Compact object masses are calculated based on 1D SN models that allow for fallback and direct BH formation, with a rapid SN engine that produces a lower-mass gap between NSs and BHs (Fryer et al. 2012). Note that for isolated binary evolution BH–BH formation, we employ models with delayed SN engines. However, as we show in Section 3.1, the choice of the SN engine model does not impact the average total BH–BH merger mass and its evolution with redshift. Massive stars (with He cores above 45 M_{\odot}) are subject to PPSNe/PSNe, and stellar-origin natal BH mass is limited to $\lesssim 45 M_{\odot}$. BH natal kicks are taken from a Maxwellian distribution with 1D $\sigma = 265 \text{ km s}^{-1}$, and kicks are decreased by fallback (i.e., there are no natal kicks for massive BHs that form through direct core collapse). This set of models assumes that BHs are born with near-zero spin, due to highly efficient angular momentum transport (e.g., Qin et al. 2018; Fuller & Ma 2019; Belczynski et al. 2020). The spin-up of massive stars (BH progenitors) by tidal interactions in close binaries is not taken into account. The stars (90%) and primordial binaries (10%) in each cluster form the first generation of BHs (with masses limited to $\lesssim 45 M_{\odot}$).

The dynamical interactions and also the mergers of BH–BH systems formed from primordial binaries produce the future generations of BHs. Obviously, these BHs can be more massive than the first generation of BHs. The second generation of BHs is typically formed with high spins ($a \sim 0.7$), due to the angular momentum of the premerger double compact object orbit. The spins of the BH remnant are calculated using the precession package (Gerosa & Kesden 2016), as described in Rodriguez et al. (2018a). Asymmetries in the BH components of the merger (unequal masses, spins) will lead to a dispersion of spin magnitudes around $a \sim 0.7$. Some second-generation BHs receive gravitational-wave recoil kicks that may remove BHs from clusters, though since the models that we consider assume that BHs are born with negligible spin, almost $\sim 60\%$ of the second-generation BHs are retained, since the recoil kicks then depend entirely on mass ratio and are typically $\lesssim 100 \text{ km s}^{-1}$ (Rodriguez et al. 2019). Those that remain bound continue to contribute to cluster evolution and to GC BH–BH merger populations. Due to the relatively low escape velocities of GCs ($\sim 30\text{--}100 \text{ km s}^{-1}$), higher-generation merger products are typically ejected from the cluster via gravitational-wave recoil kicks, due to their components having large spins as a result of their formation from previous BH–BH mergers; $\lesssim 0.1\%$ mergers containing a second-generation BH remain bound to the cluster (Rodriguez et al. 2019).

2.3. OC Dynamical Models

In this work, the long-term N -body evolutionary model set of star clusters as described in Banerjee (2021c) is utilized. The computed models are described in detail in Banerjee et al. (2020) and Banerjee (2021b, 2021c), and are summarized below.

The model star clusters, initially, have mass within $2 \times 10^4 M_{\odot} \leq M_{\text{cl}} \leq 10^5 M_{\odot}$, size (half-mass–radius) $1 \text{ pc} \leq r_{\text{h}} \leq 2 \text{ pc}$, and metallicity $0.0001 \leq Z \leq 0.02$, and they are subjected to a solar-neighborhood-like external galactic field. The initial models are composed of zero-age main-sequence (ZAMS) stars of masses $0.08 M_{\odot} \leq m_{*} \leq 150.0 M_{\odot}$ that are distributed according to the standard IMF (Kroupa 2001). About half of the models have a primordial binary population (overall initial binary fraction $f_{\text{bin}} \approx 5\%$ or 10%), where all O -type stars (stars with ZAMS mass $\geq 16 M_{\odot}$) are paired among themselves (i.e., the initial binary fraction among O -type stars is $f_{\text{Obin}} = 100\%$), following an observationally deduced distribution of massive-star binaries (Sana & Evans 2011; Sana et al. 2013; Moe & Di Stefano 2017). Such cluster parameters and stellar membership are consistent with those observed in “fully” assembled, (near-)spherical, (near-)gas-free young massive clusters, which evolve into medium-mass OCs (Portegies Zwart et al. 2010). They continue to form, evolve, and dissolve in the Milky Way and other galaxies (as such, anywhere in the universe), as a part of the galaxies’ ongoing star formation.

These model clusters evolve due to two-body relaxation (Spitzer 1987), close (relativistic) dynamical encounters (Heggie & Hut 2003; without applying any gravitational softening), and stellar evolution. This is achieved using NBODY7, a state-of-the-art post-Newtonian (PN) direct N -body integration code (Aarseth 2012; Nitadori & Aarseth 2012), which couples with the semi-analytical stellar and binary evolutionary scheme BSE (Hurley et al. 2000, 2002). As detailed in Banerjee et al. (2020), the integrated BSE is updated

in regards to the prescriptions of stellar wind mass loss and the formation of NSs and BHs. NSs and BHs form according to the “rapid” or “delayed” core-collapse SN models of Fryer et al. (2012) and the PPSN and PSN models of Belczynski et al. (2016b). The majority of the computed models of Banerjee (2021c) employ the rapid SN prescription, although a few models employ the delayed SN prescription, for exploratory purposes. The dynamical evolution and merger outcomes of the clusters are unlikely to be significantly affected by this difference, as discussed in Banerjee et al. (2020) and Banerjee (2020).

A newly formed NS or BH receives a natal kick that is modulated based on the SN matter fallback onto it, as in Belczynski et al. (2008). The adopted fallback model is that of Fryer et al. (2012). For all core-collapse SN remnants, the “base” natal kick is assigned from a Maxwellian distribution with a 1D dispersion of $\sigma = 265 \text{ km s}^{-1}$, i.e., the same velocity dispersion as that of the Galactic single-NS population (Hobbs et al. 2005). However, due to momentum conservation, the material fallback slows down the remnants, causing BHs of $\gtrsim 10 M_{\odot}$ to be retained in the clusters right after their birth. The material fallback also shapes the mass distribution of NSs and BHs. NSs formed via electron capture SNe (Podsiadlowski et al. 2004) also receive small natal kicks of a few km s^{-1} (Gessner & Janka 2018) and are retained in the clusters at birth. The present remnant scheme forms a first generation of BHs in the range $\approx 3\text{--}45 M_{\odot}$ (the upper limit set by PPSNe), and exhibits a PSN mass gap between $\approx 45\text{--}120 M_{\odot}$ (see Figure 2 of Banerjee et al. 2020). See also Banerjee et al. (2020) for further details and the description of the implementations in BSE and NBODY7.

In NBODY7, the PN treatment is handled by the ARCHAIN algorithm (Mikkola & Tanikawa 1999; Mikkola & Merritt 2008). The treatment allows for the general relativistic (GR) evolution of the innermost NS- and/or BH-containing binary of an in-cluster (i.e., gravitationally bound to the cluster) triple- or higher-order compact subsystem, in tandem with the Newtonian dynamical evolution of the subsystem (Kozai-Lidov oscillation or chaotic three-body interaction), leading to the binary’s (in-cluster) GR inspiral and potential merger. The PN treatment applies also to the GR evolution of in-cluster NS/BH-containing binaries that are not a part of a higher-order subsystem. As demonstrated in previous studies (Banerjee et al. 2010; Banerjee 2017, 2018b; Rastello et al. 2019; Banerjee 2021b), the moderate density ($10^2\text{--}10^3 \text{ stars pc}^{-3}$) and velocity dispersion ($\lesssim 10 \text{ km s}^{-1}$) in the model clusters make them efficient in dynamically assembling PN subsystems, particularly, those composed of BHs. On the other hand, the clusters’ low escape speed ($\sim 10 \text{ km s}^{-1}$) causes the dynamically ejected BH–BH systems to be typically wide (Portegies Zwart & McMillan 2000), with a GR inspiral time (Peters 1964) often exceeding the Hubble time. These cause the majority of the GR mergers from these computed clusters to be in-cluster BH–BH mergers.

In the computed models, star–star and star–remnant mergers occur due to the evolution of massive primordial binaries and three-body interactions. In the present models, a star–star merger results in the loss of $\approx 10\%$ of the total merging mass, as suggested by hydrodynamical calculations (Lombardi et al. 2002; Gaburov et al. 2008). In a BH–star merger (forming a BH–Thorne–Zytzkow Object: BH–TZO), $\approx 90\%$ of the star’s mass is taken to be accreted onto the BH. The model grid used

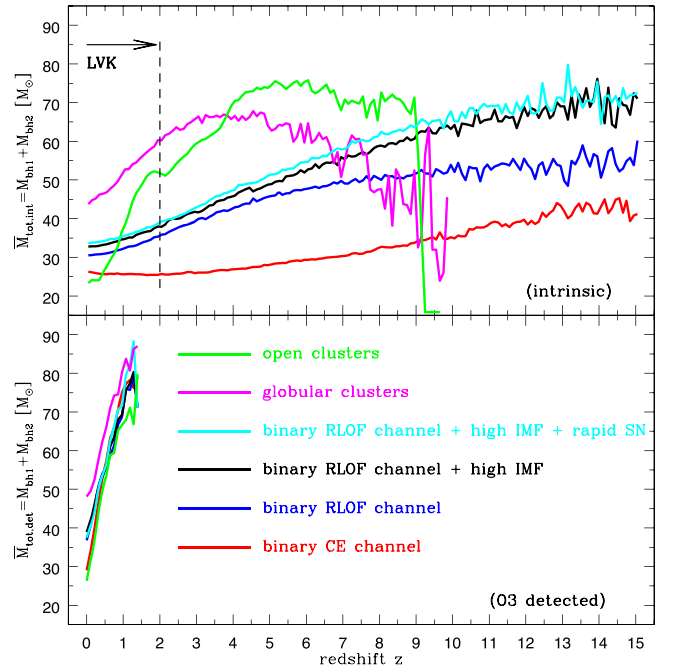


Figure 1. Top: intrinsic average total BH–BH merger mass change as a function of redshift for different BH–BH formation channels—the GC and OC dynamical channels, and the CE and RLOF isolated binary evolution channels. For the RLOF channel, we show three variations: the first allows for stars to form to $150 M_{\odot}$ and PPSNe/PSNe limit the BH masses to $\sim 55 M_{\odot}$; the second allows for star formation to $200 M_{\odot}$ and PPSNe/PSNe limit the BH masses to $90 M_{\odot}$; and the third is the same as the second variation, but employs the rapid SN engine (all the other isolated binary models employ the delayed SN engine). We show the approximate redshift range for the designed (future) LVK detection of BH–BH mergers (the range for the Einstein Telescope and the Cosmic Explorer covers the entire plot). Bottom: detected average total BH–BH merger mass change as a function of redshift. The gravitational-wave instrumental and observational selection effects are applied to the models from the top panel, to show which BH–BH mergers may be currently (due to the O3 sensitivity of LVK) detectable. Note that the rather different intrinsic curves (top) become almost indistinguishable when detection biases are applied (bottom).

in this work comprises 74 long-term ($\sim 10 \text{ Gyr}$) evolutionary cluster models (see Table A1 of Banerjee 2021c).

3. Results

3.1. Evolutionary Analysis

Our main result is shown in the top panel of Figure 1. It shows the evolution of the average intrinsic (not redshifted nor detection-weighted) total BH–BH mass ($\overline{M}_{\text{tot,int}} = M_{\text{bh1}} + M_{\text{bh2}}$) with redshift (z). The evolution is shown for the six models (see Section 2) of BH–BH merger formation: the GC dynamical channel, the OC dynamical channel, the classical CE isolated binary evolution channel, the RLOF isolated binary evolution channel, the extended RLOF channel (with more massive stars and BHs), and the extended RLOF channel with the rapid SN engine.

Within the approximate LVK-designed redshift range for the detection of BH–BH mergers ($z < 2$),⁸ the CE channel produces the lowest-mass BH–BH mergers ($\overline{M}_{\text{tot,int}} \sim 25 M_{\odot}$, irrespective of the redshift), the three RLOF channels produce more massive BH–BH mergers, which show a slow increase of the average mass with increasing redshift, as the metal-poor

⁸ The maximum detectable redshift of a $50M_{\odot}\text{--}50M_{\odot}$ BH merger with Advanced LIGO at the design sensitivity is $z_h = 1.9$, as calculated with the gravitational-wave distance calculator described in Chen et al. (2021).

environments at higher redshifts produce more massive BHs ($\bar{M}_{\text{tot,int}} \sim 30 \rightarrow 35 M_{\odot}$ for $z=0 \rightarrow 2$), and the GC channel produces the most massive BH–BH mergers, with a fast increase of the average mass with redshift ($\bar{M}_{\text{tot,int}} \sim 45 \rightarrow 60 M_{\odot}$ for $z=0 \rightarrow 2$). The OC channel generates the most dramatic evolution of the intrinsic average total BH–BH merger mass ($\bar{M}_{\text{tot,int}} \sim 25 \rightarrow 50 M_{\odot}$ for $z=0 \rightarrow 2$).

In the entire presented redshift range ($z < 15$) that will be accessible to the Einstein Telescope and the Cosmic Explorer, the four isolated binary evolution channels produce gradually more massive BH–BH mergers with increasing redshift (at $z=15$, we find: $\bar{M}_{\text{tot,int}} \sim 40 M_{\odot}$ for the CE channel, $\bar{M}_{\text{tot,int}} \sim 55 M_{\odot}$ for the RLOF channel, and $\bar{M}_{\text{tot,int}} \sim 70 M_{\odot}$ for both the RLOF channels with extended IMF). For BH–BH mergers in the GC channel, we find that the average mass first increases with redshift (reaching a maximum of $\bar{M}_{\text{tot,int}} \sim 65 M_{\odot}$ at $z=3-5$), then gradually decreases with increasing redshift. For the OC channel, we find that the average BH–BH mass first increases with redshift, reaching high values ($\bar{M}_{\text{tot,int}} \sim 70 M_{\odot}$ at $z=4-9$), then sharply decreases for higher redshifts.

The general increase of the intrinsic average BH–BH mass with redshift for all four isolated binary evolution channels is easily understood in the framework of cosmic chemical evolution. The chemical composition of stars (i.e., metallicity, Z) is the primary factor setting the mass of stellar-origin BHs (Belczynski et al. 2010a). At lower metallicities, stellar winds are weaker (which removes mass from stars), and more massive BHs are able to form. Since metallicity decreases with redshift, more massive stellar-origin BHs form at higher redshifts. There is an exception to this general trend for the CE BH–BH formation channel at low redshifts ($z \lesssim 2-3$), where the BH–BH merger total mass remains constant and does not change with redshift. We explain this behavior in Appendix A.

The lowest average total BH–BH merger mass (at any redshift) is found for the CE BH–BH binary formation channel. The actual value of the average mass is a combination of the adopted stellar wind mass loss for massive stars and their dependence on metallicity, the cosmic evolution of metallicity with redshift, and the specific evolutionary sequences (set by stellar/binary input physics assumptions) producing BH–BH mergers in the CE binary channel. The RLOF binary channel produces on average more massive BH–BH mergers. Since the wind mass loss and cosmic metallicity evolution for this channel are the same as for the CE channel, the entire difference in the average total mass originates from different stellar/binary evolutionary assumptions. We explain the (nontrivial) origin of this difference in Appendix B. Finally, the two RLOF models with high (extended) IMF naturally produce the most massive BH–BH mergers among our isolated binary models. In these two models, BHs may form up to $90 M_{\odot}$, as compared to a maximum mass of a BH of $\sim 55 M_{\odot}$ in the other two binary models. We note slightly larger total BH–BH masses (\lesssim few M_{\odot}) for the model with the rapid SN engine, as the BHs that would form in the lower-mass gap in the delayed SN engine model are simply forming with masses just above the mass gap. Note that the small differences between these two models with extended IMF but different SN engines are much smaller than the differences associated with the BH–BH formation mode (the CE versus RLOF channels) or the changes of the IMF and PPSN/PSN models.

The GC channel produces on average significantly more massive BH–BH mergers at low and intermediate redshifts

($z < 5$) compared to any presented isolated binary evolution model by about $\bar{M}_{\text{tot,int}} \sim 10-20 M_{\odot}$ (see Figure 1). This is due to the most massive BHs in the cluster more readily synthesizing binaries through dynamical interactions, as well as the contribution of mergers containing a second-generation BH that was retained in the cluster following its first merger. The average total merger mass drops at high redshifts ($z \gtrsim 7$), when GC BH–BH mergers become more dominated by BH–BH mergers from primordial binaries.

Unlike the isolated evolution channels considered, the GC model has a peak in the average mass of BH–BH mergers near the peak of GC formation, at redshifts of $z \sim 3-5$. The most massive BHs in the cluster ($\gtrsim 20 M_{\odot}$) are typically the first to be dynamically processed, either merging in the cluster at early times or being ejected and inspiraling over longer timescales. Less massive BHs born in the clusters ($\sim 10-15 M_{\odot}$) follow suit, and typically merge at later times than their more massive counterparts, leading to the decrease in the average total mass at lower redshifts ($z \lesssim 3$). At $z \gtrsim 5$, the primordial binaries in the cluster that evolve and lead to BH–BH mergers that were formed in quasi-isolation (without much assistance from dynamical interactions) have a larger contribution to the total population of BH–BH mergers, driving the overall decline in the average mass at large redshifts. These systems rapidly merge on timescales shorter than the mass-segregation timescale in their GC hosts of $\mathcal{O}(100 \text{ Myr})$. However, dynamically processed mergers still occur at these higher redshifts, which, combined with the small number statistics (GCs are just beginning to form), leads to the fluctuating behavior in the average total mass evolution at $z \gtrsim 5$. The relative contribution of BH mergers from quasi-isolated evolution prior to the peak of GC formation and their impact on the average mass change with redshift depends on the metallicity evolution of the cluster formation, which is distinct from the metallicity evolution of isolated binaries in galactic fields.

Interpretation along lines similar to the case of GCs applies to the evolution of the average total mass with merger redshift for OCs (Figure 1; top panel). However, a twist for OCs is that such systems, being 1–2 orders of magnitude less populous than, but of similar (initial) length scale as, GCs, have a shorter two-body relaxation time (Spitzer 1987) compared to GCs of a factor of a few to tens. In OCs, the most massive BHs/BH progenitors segregate to the cluster center in $\lesssim 10 \text{ Myr}$ (see Banerjee 2021a). Also, before the formation of BHs, a fraction of the BH progenitors already undergo complete mass segregation, due to the shorter relaxation/mass-segregation timescale. These cause the dynamical processing and mergers among BHs to commence at earlier ages (i.e., at larger redshifts) and closer to the quasi-isolated mergers in OCs than in GCs. Also, due to the smaller member number, and hence primordial binary population, in OCs, the models produce a much smaller number of quasi-isolated BH–BH mergers per cluster than the GC models (Fragione & Banerjee 2020).

The effects of these differences in OCs can be seen in Figure 1. As opposed to GCs, the $\bar{M}_{\text{tot,int}}$ for OCs rises sharply at $z \approx 9$ (fewer quasi-isolated mergers), thereafter remaining nearly flat and peaking weakly between $5 < z < 6$ (pre-/faster mass segregation), before dropping off toward low z faster than GCs (faster dynamical processing, due to shorter relaxation times in OCs). It is also to be noted that the OCs are taken to follow a different metallicity-dependent cosmic star formation history (Chruslinska & Nelemans 2019; their “moderate-Z”

relation—see Banerjee (2021c) for details) than those for both the isolated binary and GC models presented here, which would also cause differences in the redshift dependence of $\bar{M}_{\text{tot,int}}$. Although OCs are inefficient in producing massive BHs via hierarchical mergers, the computed OC models adopt a small, $\approx 10\%$, mass loss in star–star mergers (based on hydrodynamic stellar merger calculations; see Section 2.3), which is the main channel for forming the most massive BHs lying within the PPSN/PSN mass gap in these models (Banerjee 2021b, 2021a). Furthermore, a 90% BH–TZO accretion is adopted (Section 2.3). These, along with the tendency of having lower metallicity at high redshifts than GC or binary models, results in a higher maximum $\bar{M}_{\text{tot,int}}$ for OCs (Figure 1).

3.2. Comparison to Observed Gravitational Waves

Although all the models explored in this work show notable differences in the average total mass of the mergers and its evolution with redshift (the only exceptions being the two RLOF models with an extended IMF: one with a rapid and one with a delayed SN engine), there is no guarantee that these differences can be measured with current gravitational-wave sensitivity. First, gravitational-wave sources are subject to strong selection effects, which not only limit the distance to which BH–BH mergers can be detected, but also preferentially enable the detection of certain binary mass and spin configurations. As a result, the properties of the detected population of BH–BH mergers will not match those of the intrinsic population. Furthermore, gravitational-wave detectors are subject to a variety of sources of noise, so the true masses, spins, and distances of detected events can only be estimated, often with sizable uncertainties. Finally, we are still in the era of small number statistics when it comes to gravitational-wave detections, so even if the true properties of a detected system were known, there still exists a counting uncertainty in the number of similar events occurring in the universe.

Given these combined effects, as well as the poorly understood systematic uncertainties in the six population synthesis models presented here, we take a simple approach to assessing whether these models are distinguishable with current detections, and whether any of them are a reasonable fit to the data, in analog to the investigations in Fishbach et al. (2021). In Figure 2, we show the average *detected* mass $\bar{M}_{\text{tot,det}}$ as a function of redshift under each of our six models, by computing the average detected total mass in 14 equally spaced redshift bins (i.e., 15 bin edges) from $z=0$ to $z=1.5$. These curves are also reproduced in Figure 1 for comparison to the intrinsic average masses. $\bar{M}_{\text{tot,det}}$ is essentially $\bar{M}_{\text{tot,int}}$ filtered through the LVK detector and analysis selection function. To simulate these effects of the detector and the analysis selection bias on the detected populations, we reweight the detected software injections provided in the LIGO Scientific Collaboration (2021c) by the intrinsic simulated populations. To perform the reweighting, a histogram of the population synthesis samples from each model is used to approximate the intrinsic simulated population probability distribution over masses and redshifts.

The model curves in Figure 2 show the average detected total mass increasing as a function of redshift, which is expected, given that the less massive sources are more detectable out to lower redshifts than the more massive

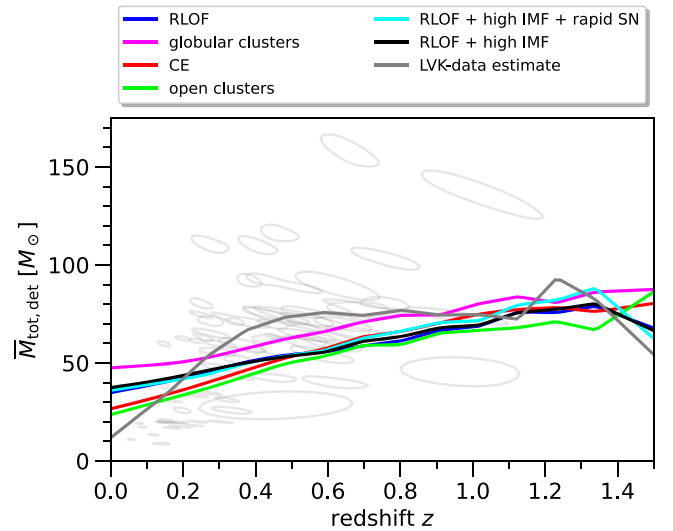


Figure 2. The average detected total mass as a function of redshift for the six models considered in this work. The models are overlaid on the gray 90% credible interval parameter regions for BH–BH mergers from LVK O3, reweighted to an astrophysically realistic prior. The gray line shows an estimate of the mean detected total mass of these events in different redshift bins for all posterior samples under the aforementioned prior.

sources. The rate of change of the average detected total mass with redshift is approximately the same for all our models, though the CE channel shows the strongest increase with redshift. To compare these curves to those in Figure 1, consider that the slopes of the $\bar{M}_{\text{tot,det}}$ lines are strongly influenced by the selection effects, which will increase the lowest detectable mass with increasing redshift, and therefore force models with low constant intrinsic average mass, like the CE channel, to appear to evolve with redshift in the detected population. In contrast, for the OCs, the average intrinsic mass changes from ~ 25 to $\sim 50 M_{\odot}$ between redshift 0 and 1, which matches what is seen in the detected average mass. This means that the true average mass evolution with redshift in the OC model roughly follows the O3 LVK selection effects. The similarity between the slopes of the $\bar{M}_{\text{tot,det}}$ curves suggests that the changes in the total mass distribution mean over redshift are not good distinguishers of these models, given the current sensitivity. However, the overall mass scale is more telling: the GC model predicts a higher average detected mass than the other models by ~ 10 – $20 M_{\odot}$, regardless of redshift.

To compare these simulated average detected masses to the masses of detected BH–BHs, we overlay in gray the 90% credible regions on detector-frame total mass and redshift for the BH–BH systems in GWTC-3 from the third LVK observing run (Abbott et al. 2021a, 2021b; The LIGO Scientific Collaboration 2021a). Only BH–BH mergers from O3 are selected, for a uniform sample. The credible regions are generated via kernel density estimates of the posterior samples provided by LVK, reweighted to a prior that approximates the empirical measurements of the merger population distribution (Roulet et al. 2021; The LIGO Scientific Collaboration 2021b; The LIGO Scientific Collaboration 2021c). Specifically, we use (1) a broken power-law prior on the more massive BH in the binary’s mass, with $p(m_1) \propto m_1^{-1.7}$ for $m_1 < 40 M_{\odot}$, and $p(m_1) \propto m_1^{-5}$ for $m_1 \geq 40 M_{\odot}$; (2) a $p(q) \propto q$ prior for the mass ratio q ; and (3) a uniform-in-comoving-time volume prior on z ,

i.e., $p(z) \propto \frac{dV}{dz} \frac{1}{1+z}$. Additionally, we estimate the mean mass of these detections over redshift by computing a single total mass mean from the combined samples of all the events in the same redshift bins used for the six models' curves. We show this estimate in gray in Figure 2.

At $z \sim 0.5$, all the models appreciably underpredict the estimated mean detected mass by $\sim 25 M_{\odot}$, except GC, which underpredicts by $\sim 10 M_{\odot}$. This is consistent with the fact that the GC model is the only model with a non-negligible fraction ($>1\%$) of systems with $M_{\text{tot,int}} > 100 M_{\odot}$ below $z = 1$. At the highest redshifts, it is not clear which model(s) may fit the data well, given that there are few events detected at these distances, and those events have large uncertainties and low significance. At redshifts less than ~ 0.2 , all the models overpredict the average detected mass. This is simply because none of the models predict a sufficiently high rate of low-mass mergers. Overall, these findings, especially at low masses and redshifts, suggest that none of these models alone (or even a mixture of them) are a good fit to GWTC-3 events. However, the GC model offers the closest $\bar{M}_{\text{tot,det}}$ prediction for high-redshift events, but would require either a different set of input physics or another channel, also with a different set of input physics than explored in this work, to fill in the low and high ends of the mass distribution.

We emphasize that the explorations here are primarily illustrative. None of the models herein have been tuned to fit the LVK data, nor have we performed a simultaneous fit to all binary parameters in the LVK catalog, accounting for measurement uncertainties. However, comparisons such as the one shown in Figure 2 will be invaluable for assessing the viability of BH–BH formation channel models and will enable a narrowing of the parameter space for easier follow-up studies that perform a complete statistical analysis.

4. Conclusions

We have employed several BH–BH merger formation models to show the evolution of the average intrinsic and detected total BH–BH merger mass with redshift. Our main results are shown in Figures 1 and 2. In our analysis, we have included the classical isolated binary CE evolution formation channel, three stable RLOF channels—one with a standard IMF (stars with masses $< 150 M_{\odot}$ and PPSNe/PSNe limiting BH masses to $< 55 M_{\odot}$) and two with an extended IMF (stars with masses $< 150 M_{\odot}$ and PPSNe/PSNe limiting BH masses to $< 90 M_{\odot}$), but with different SN engines (delayed and rapid)—and GC and OC dynamical BH–BH formation channels.

The model differences in average intrinsic BH–BH total mass are both quantitative and qualitative. The lowest average masses are produced by the CE binary channel ($\bar{M}_{\text{tot,int}} \sim 25 M_{\odot}$ at $z = 0-2$), with somewhat larger masses found for the RLOF channels ($\bar{M}_{\text{tot,int}} \sim 30 M_{\odot}$ at $z = 0$, and increasing to $\sim 35 M_{\odot}$ at $z = 2$). The largest masses in the LVK range are produced by GCs ($\bar{M}_{\text{tot,int}} \sim 45 M_{\odot}$ at $z = 0$, with a notable increase to $\sim 60 M_{\odot}$ at $z = 2$). OC BH–BH mergers show the most pronounced evolution of the average total mass in this redshift range ($\bar{M}_{\text{tot,int}} \sim 25 M_{\odot}$ at $z = 0$ and $\sim 50 M_{\odot}$ at $z = 2$), bridging the isolated binary and GC models.

These differences become more pronounced for higher redshifts. The isolated binary channels show a monotonic increase of the average intrinsic BH–BH merger mass with redshift, with the exception that, for the CE channel, the average intrinsic mass is constant for low redshifts ($z \lesssim 2-3$),

then increases with increasing redshift. A different behavior is found for the GC model, for which the average intrinsic merger mass increases with redshift to $z \sim 4$, then decreases with redshift. The OC model shows similar behavior to the GC model, but the largest intrinsic total BH–BH masses are produced at higher redshifts ($\bar{M}_{\text{tot,int}} \gtrsim 70 M_{\odot}$ for $z \sim 5-9$). These trends are understood in the framework of the input physics employed in the models (see Section 3.1 for details).

We have shown that not only the formation channel (e.g., isolated binary versus cluster BH–BH formation) significantly affects the intrinsic average BH–BH merger mass, but that some parts of the highly uncertain input physics within a given formation channel have big impact. For example, changing the CE development criteria for the isolated binary evolution channel significantly impacts the BH–BH merger formation mode (CE versus RLOF) and the intrinsic total BH–BH merger mass. A similar statement can be made about the impact of the treatment of PPSNe/PSNe and the extent of the IMF in binary evolution calculations. However, not all of the input physics is that important for the intrinsic average total BH–BH merger mass and its evolution with redshift. For example, an SN engine model that regulates the existence and numbers of compact objects with masses in the lower-mass gap ($\sim 2-5 M_{\odot}$) does not significantly impact the intrinsic average total BH–BH merger mass. Since all these parts of the physics of BH–BH merger formation (CE, SN engine, PPSN/PSN) are highly uncertain, we adopted models with various assumptions on the parameters regulating these processes.

The evolution of the averaged detected BH–BH merger total mass does not differ as much between formation channels compared to the intrinsic mass (see Figure 2). The four binary models and the OC model show similar behaviors for redshifts in which mergers are currently detected ($z \lesssim 1$). Only the GC model results in moderately heavier detected BH–BH mergers (by $\lesssim 10 M_{\odot}$ for $z \lesssim 1$). This is caused by LVK detection biases, which affect different models in different ways (as explained in Section 3.2). These differences in mass evolution with redshift are too small to differentiate between models with the current LVK data, due to the large detection errors. Additionally, none of the employed models match the average detected BH–BH merger masses over the entire BH–BH detectable redshift range. However, the adopted GC model matches the current data better than our isolated binary or OC models at moderate redshifts $z \sim 0.5$.

The physics of BH–BH merger progenitors for isolated binary, GC, and OC formation channels is still subject to many uncertainties (Conroy & Gunn 2010; Chatterjee et al. 2017; Santoliquido et al. 2021; Belczynski et al. 2022). Major overall uncertainties include the underlying cosmic star formation rate of isolated binaries and stars/binaries in GCs and OCs, and the metallicity evolution with redshift (Sharda et al. 2021) within each formation channel (Neijssel et al. 2019). Basic stellar evolution uncertainties include fusion reaction rates (Fields et al. 2018), the mixing in stellar interiors (Zhang 2013), stellar wind mass-loss rates (Björklund et al. 2022), radial expansion, and the core-collapse/SN physics (Schneider et al. 2019) associated with compact object formation (Belczynski et al. 2022), as well as the initial conditions, such as the IMF, mass ratio, orbital separation, and eccentricity (Klencki et al. 2018). Binary evolution physics is highly uncertain in its treatment of stellar interactions, whether these are stable or unstable (CE) RLOF events (Dominik et al. 2012; Ablimit & Maeda 2018). In

the modeling of dynamical BH–BH formation, the unknown initial conditions of GCs and OCs (size, density, binary fractions), along with the uncertain outcomes of stellar mergers and BH (natal and gravitational-wave) kicks, hinder their predictions.

Keeping these uncertainties in mind, we can deliver only a very limited conclusion. For some choices of input physics in a given BH–BH formation channel (the six presented models), we predict that the average intrinsic total BH–BH merger mass evolution with redshift changes from model to model, sometimes in rather significant ways. However, due to the BH–BH detection selection effects, the small statistics of the detected sources, and the significant uncertainties in the detected BH–BH masses and redshifts, the current LVK O3 data does not enable us to identify any model as fitting the data better than another. Additionally, no models (or their potential combinations) fit the entirety of the data well, due to their dearth of low-mass events relative to the detected population. More data from LVK in O4 and O5 may change this conclusion. At this moment, it is clear that the average total mass (and its evolution with redshift) may be very different for the various formation models, and this may help in the future to eliminate some models and to support others, as well as guide theoretical work on the physics of BH–BH merger progenitors. The total BH–BH merger mass and its evolution with redshift may provide, along with other observables, extra leverage in the search for the BH–BH formation site/channel.

K.B. and A.O. acknowledge support from the Polish National Science Center grant Maestro (2018/30/A/ST9/00050). Z.D. is supported by the CIERA Board of Visitors Research Professorship. Support for M.Z. is provided by NASA, through the NASA Hubble Fellowship grant HST-HF2-51474.001-A, awarded by the Space Telescope Science Institute, which is operated by the Association of Universities for Research in Astronomy, Incorporated, under NASA contract NAS5-26555. D.C. is supported by the STFC grant ST/V005618/1. S.B. acknowledges support from the Deutsche Forschungsgemeinschaft (DFG; German Research Foundation) through the individual research grant “The dynamics of stellar-mass black holes in dense stellar systems and their role in gravitational-wave generation” (BA 4281/6-1; PI: S. Banerjee). S.B. acknowledges the generous support and efficient system maintenance of the computing teams at AIfA and HISKP. This work was initiated and performed in part at the Aspen Center for Physics, which is supported by National Science Foundation grant PHY-1607611. This material is based upon work supported by NSF’s LIGO Laboratory, which is a major facility fully funded by the National Science Foundation.

Appendix A

All four binary models show a general increase in the average intrinsic total BH–BH merger mass with redshift (see Figure 1). However, there is an exception to this trend, for the CE BH–BH formation channel at low redshifts ($z \lesssim 2-3$). Here, we provide an explanation for this behavior.

For this channel, BH–BH merger formation depends sensitively on the radial expansion of BH progenitor stars, and thus on metallicity (Belczynski et al. 2010b). For our CE model, we only allow CEs to develop and successfully form

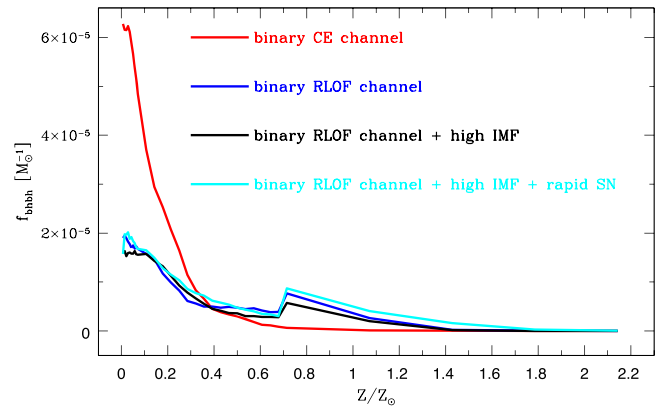


Figure 3. BH–BH merger formation efficiency per unit mass as a function of metallicity for the CE and three RLOF isolated binary evolution channels.

close binaries at late-donor evolutionary stages (e.g., during core He burning). Significant radial expansion during core He burning is found at low metallicity, as high-metallicity H-rich stellar envelopes are usually severely depleted by stellar winds for massive stars. As the metallicity of stellar populations increases with decreasing redshift, the CE-channel BH–BH merger formation efficiency significantly drops, as seen in Figure 3. For low redshifts ($z \lesssim 2-3$), the average metallicity of the stellar populations becomes significant ($Z > 0.5 Z_\odot$; see Figure 7 of Belczynski et al. 2020), and the formation efficiency of BH–BH mergers is very small. The low-mass BH–BH mergers that form from high-metallicity stars do not contribute significantly to the overall population of BH–BH mergers at these redshifts. The majority of the mergers at these redshifts originate from low-metallicity stars that still form in the tail of the metallicity distribution, even to $z = 0$. Massive mergers that form at low metallicity at high redshifts do not contribute significantly at low redshifts, as merger rates fall off steeply with delay time (Dominik et al. 2012). This sharp drop in the BH–BH merger formation efficiency with metallicity (Figure 3) is responsible for the flat behavior of the average BH–BH merger mass at low redshifts. This does not affect the RLOF channels, as they depend on the expansion of stars at much earlier evolutionary stages (e.g., during the Hertzsprung gap), which are not affected as much by stellar winds and metallicity.

Appendix B

Here, we explain the difference in the average total mass of BH–BH mergers between the CE formation channel and the RLOF channels. It is clearly visible that the RLOF channels produce much more massive BH–BH mergers at all redshifts (see Figure 1).

In Figures 4 and 5, we present formation scenarios for typical BH–BH mergers at redshift $z = 6$ in the CE and stable RLOF (standard IMF, delayed SN engine) isolated binary evolution channels, respectively. The two chosen examples of BH–BH systems have their total mass and metallicity close to the average mass $M_{\text{tot,int}} = 29.3, 47.7 M_\odot$ (CE, RLOF) and the average metallicity $Z = 0.0013, 0.0012$ (CE, RLOF) at $z = 6$ for the two channels (see Figure 6). For the CE channel, we show an example with $M_{\text{tot,int}} = 31 M_\odot$, and for the standard RLOF channel with $M_{\text{tot,int}} = 47 M_\odot$. Note the very clear total mass difference of the BH–BH mergers from the two formation scenarios. Below, we explain the origin of this difference.

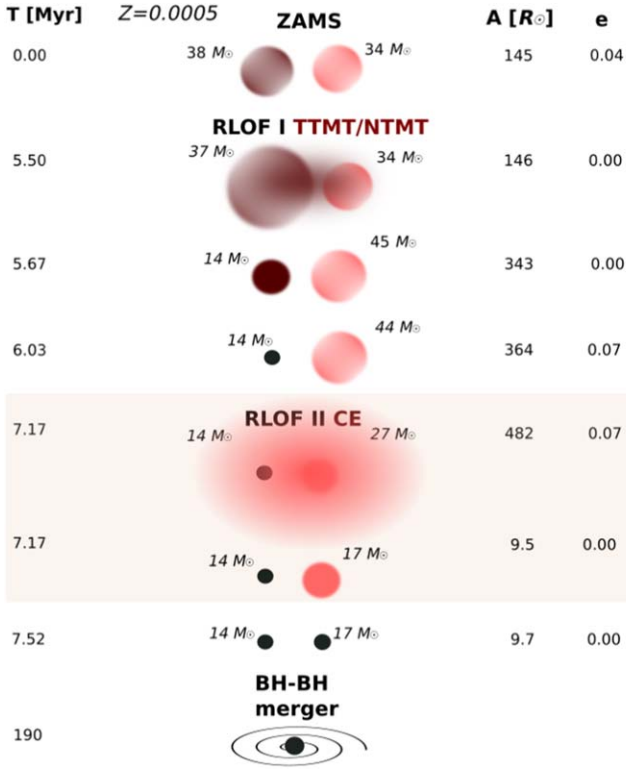


Figure 4. The formation scenario for a typical BH–BH merger at redshift $z \approx 6$ in the classical (CE) isolated binary evolution channel. The shaded part of the evolution shows the most important part of the evolution, which leads to orbital decay, allowing for the formation of a close BH–BH binary that can merge in the Hubble time.

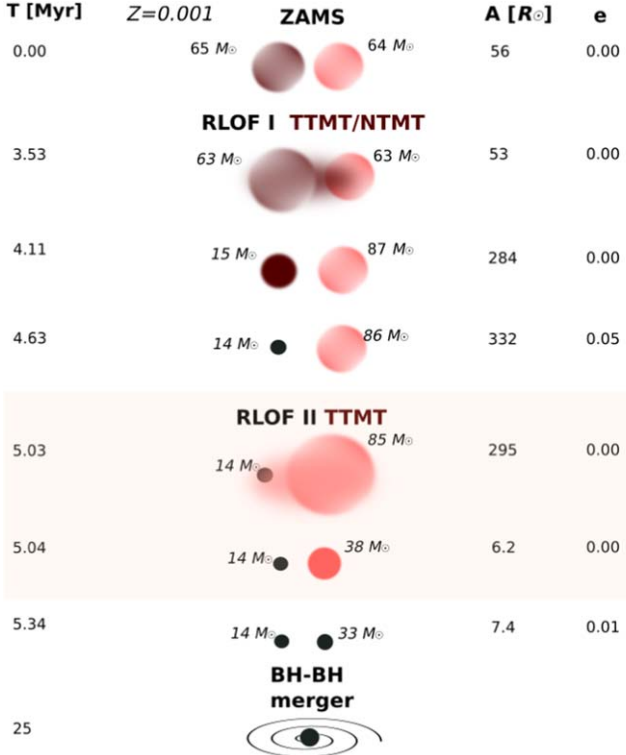


Figure 5. The formation scenario for a typical BH–BH merger at redshift $z \approx 6$ in the stable RLOF channel (standard IMF, delayed SN engine). The shaded part of the evolution shows the most important part of the evolution, which leads to orbital decay, allowing for the formation of close BH–BH binary that can merge in the Hubble time.

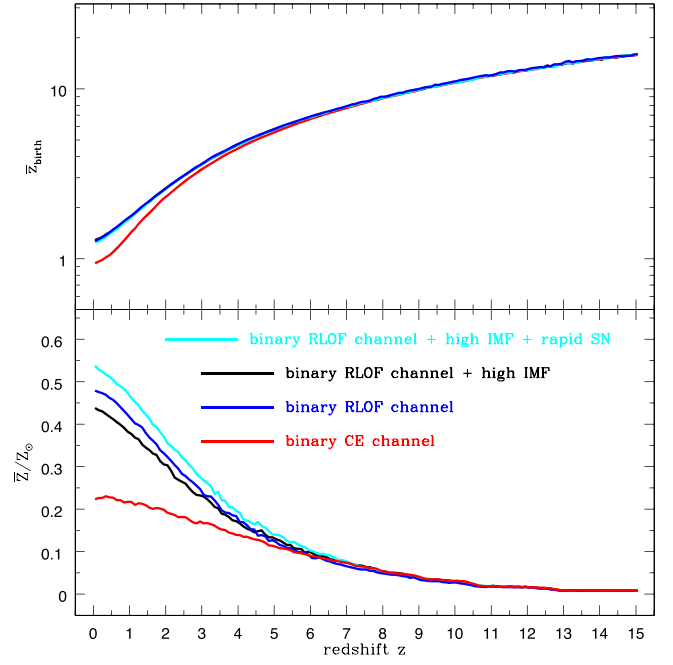


Figure 6. Top: average birth redshift of the binary progenitors of BH–BH mergers that merge at a given redshift for four isolated binary formation channels. Note that the black and cyan lines are right under the blue line. Bottom: average metallicity of binaries that produce BH–BH mergers at a given redshift.

The two examples, despite having rather different primary stars ($\sim 38 M_{\odot}$ and $\sim 65 M_{\odot}$ at ZAMS: $t = 0$ Myr), produce BHs of similar mass ($\sim 14 M_{\odot}$) out of the primary stars. This comes from the fact that both primaries are stripped of their H-rich envelopes (the first RLOF phase in each case) at different evolutionary stages, and their exposed helium cores, WR stars, have almost the same mass. In the CE scenario, the first RLOF begins when the primary is in the Hertzsprung gap, and its helium core is developed after the entirety of main-sequence H burning. In the RLOF scenario, the first RLOF begins when the primary is still in the main sequence, and, due to mass loss, the star is derejuvenated, producing a much smaller core than would be expected for a single star with the same initial mass. Since both first-formed BHs have the same mass, this means that the mass difference between the two BH–BH mergers is directly connected to the secondary star, its mass, and its evolution.





In the CE channel, the secondary mass is $34 M_{\odot}$ at $t = 0$ Myr. It increases to $45 M_{\odot}$ after the first stable RLOF event. The secondary then loses mass in stellar winds to initiate the second RLOF, at a mass of $27 M_{\odot}$, when it is core He burning. This second RLOF is a CE event that leaves the secondary as a naked helium core (a WR star), with a mass of $17 M_{\odot}$, which quickly collapses to a BH with similar mass. Note the significant orbital separation decay during the CE phase, from $a = 482 R_{\odot}$ to $a = 9.5 R_{\odot}$. If we made the binary at this stage proceed through stable RLOF instead, then there would not be enough orbital contraction to produce a merging BH–BH system. Simply, the secondary star would not have enough mass in its envelope to allow for enough associated angular momentum loss from the binary to provide significant orbital decay. The orbital decay would be rather small, from $a = 482 R_{\odot}$ to $a = 440 R_{\odot}$, producing a BH–BH system with an inspiral time much larger than the Hubble time.

In the RLOF channel, the secondary starts with a mass of $64 M_{\odot}$. It increases to $87 M_{\odot}$ after the first stable RLOF event. Then the secondary, with almost no mass loss— $85 M_{\odot}$ (mostly main-sequence evolution, with a relatively small stellar radius)—initiates the second RLOF event right after the main sequence, when it is in the Hertzsprung gap. The second RLOF is a stable thermal timescale mass transfer. The RLOF strips the secondary of its envelope, leaving a WR star with a mass of $38 M_{\odot}$. After losing about $5 M_{\odot}$ to winds, the WR star collapses to a massive BH of $33 M_{\odot}$. This second RLOF event reduces the orbital separation from $a = 295 R_{\odot}$ to $a = 6.2 R_{\odot}$, producing a close BH–BH system that can merge in the Hubble time. The high mass of the donor star (secondary) in this event is required to allow for the significant decay of the orbit. During thermal timescale mass transfer, almost the entirety of the donor’s envelope is lost from the binary (due to a highly over-Eddington mass transfer rate), taking away the binary angular momentum and reducing the size of the orbit (as long as the donor mass is larger than the accretor mass). In order to form a BH–BH binary system close enough to merge in the Hubble time through two stable RLOF episodes, the donor star needs to be a few times more massive than its BH companion at the onset of the second RLOF event (van den Heuvel et al. 2017; Olejak et al. 2021). Only such unequal-mass binaries ($q_{\text{RLOF}} = \frac{M_{\text{don}}}{M_{\text{acc}}} \gtrsim 3$) are able to eject a large enough amount of mass and orbital angular momentum to reduce the orbital separation enough to produce merging BH–BH systems.

If, at the onset of the second RLOF event, we applied CE evolution instead of stable mass transfer, then the ejection of the very massive envelope of the secondary ($47 M_{\odot}$) would lead to post-CE separation of only $a = 0.7 R_{\odot}$. This is smaller than the radius of a secondary core (a WR star: $>1\text{--}2 R_{\odot}$; Hurley et al. 2000), and thus CE evolution would lead to a merger of the BH with the massive secondary and no formation of a BH–BH system. Note that in our standard simulations, we would not even attempt to perform CE evolution for such a case, as the donor (secondary) is in the Hertzsprung gap at the onset of RLOF and has a radiative envelope that would not allow for the development/survival of a CE (Belczynski et al. 2007; Klencki et al. 2021).

Of course, to alleviate this issue, one may require the formation of a much wider binary at the onset of the second RLOF event. Then, not only would there be enough orbital energy to successfully expel the CE, but the donor star would also be core He burning and much more extended, as well as having a convective envelope. However, such a star has already evolved through most its life and lost a significant fraction of its H-rich envelope through stellar winds. In such a case, even very efficient CE evolution may not be enough to decay the orbit below the threshold of formation for merging BH–BH systems. It is possible, but it requires fine tuning, and for a given model of CE efficiency and adopted stellar winds, only a few systems form massive BH–BH mergers in the CE channel. This has already been proposed and explained, although in somewhat different terms, by van Son et al. (2022), and our detailed description is provided only to serve as a replication study.

ORCID iDs

Zoheyr Doctor  <https://orcid.org/0000-0002-2077-4914>
 Michael Zevin  <https://orcid.org/0000-0002-0147-0835>
 Aleksandra Olejak  <https://orcid.org/0000-0002-6105-6492>
 Sambaran Banerjee  <https://orcid.org/0000-0002-1254-2603>

References

- Aarseth, S. J. 2012, *MNRAS*, **422**, 841
 Abbott, R., Abbott, T. D., Abraham, S., et al. 2021a, *PhRvX*, **11**, 021053
 Abbott, R., Abbott, T. D., Acernese, F., et al. 2021b, *PhRvX*, **11**, 021053
 Ablimit, I., & Maeda, K. 2018, *ApJ*, **866**, 151
 Antonini, F., & Gieles, M. 2020, *PhRvD*, **102**, 123016
 Antonini, F., Toonen, S., & Hamers, A. S. 2017, *ApJ*, **841**, 77
 Arca Sedda, M. 2020, *ApJ*, **891**, 47
 Arca Sedda, M., Askar, A., & Giersz, M. 2018, *MNRAS*, **479**, 4652
 Arca Sedda, M., & Benacquista, M. 2019, *MNRAS*, **482**, 2991
 Arca-Sedda, M., & Capuzzo-Dolcetta, R. 2017, *MNRAS*, **471**, 478
 Askar, A., Szkudlarek, M., Gondek-Rosińska, D., Giersz, M., & Bulik, T. 2017, *MNRAS*, **464**, L36
 Banerjee, S. 2017, *MNRAS*, **467**, 524
 Banerjee, S. 2018a, *MNRAS*, **473**, 909
 Banerjee, S. 2018b, *MNRAS*, **481**, 5123
 Banerjee, S. 2020, *PhRvD*, **102**, 103002
 Banerjee, S. 2021a, arXiv:2109.14612
 Banerjee, S. 2021b, *MNRAS*, **500**, 3002
 Banerjee, S. 2021c, *MNRAS*, **503**, 3371
 Banerjee, S., Baumgardt, H., & Kroupa, P. 2010, *MNRAS*, **402**, 371
 Banerjee, S., Belczynski, K., Fryer, C. L., et al. 2020, *A&A*, **639**, A41
 Bavera, S. S., Fragos, T., Zevin, M., et al. 2021, *A&A*, **647**, A153
 Belczynski, K. 2020, *ApJL*, **905**, L15
 Belczynski, K., Bulik, T., Fryer, C. L., et al. 2010a, *ApJ*, **714**, 1217
 Belczynski, K., Dominik, M., Bulik, T., et al. 2010b, *ApJL*, **715**, L138
 Belczynski, K., Holz, D. E., Bulik, T., & O’Shaughnessy, R. 2016a, *Natur*, **534**, 512
 Belczynski, K., Kalogera, V., & Bulik, T. 2002, *ApJ*, **572**, 407
 Belczynski, K., Kalogera, V., Rasio, F. A., et al. 2008, *ApJS*, **174**, 223
 Belczynski, K., Taam, R. E., Kalogera, V., Rasio, F. A., & Bulik, T. 2007, *ApJ*, **662**, 504
 Belczynski, K., Wiktorowicz, G., Fryer, C. L., Holz, D. E., & Kalogera, V. 2012, *ApJ*, **757**, 91
 Belczynski, K., Heger, A., Gladysz, W., et al. 2016b, *A&A*, **594**, A97
 Belczynski, K., Klencki, J., Fields, C. E., et al. 2020, *A&A*, **636**, A104
 Belczynski, K., Romagnolo, A., Olejak, A., et al. 2022, *ApJ*, **925**, 69
 Björklund, R., Sundqvist, J. O., Singh, S. M., Puls, J., & Najarro, F. 2022, arXiv:2203.08218
 Broekgaarden, F. S., Berger, E., Stevenson, S., et al. 2022, *MNRAS*, *stac1677*
 Chatterjee, S., Rodriguez, C. L., & Rasio, F. A. 2017, *ApJ*, **834**, 68
 Chattopadhyay, D., Hurley, J., Stevenson, S., & Raidani, A. 2022, *MNRAS*, **513**, 4527
 Chen, H.-Y., Holz, D. E., Miller, J., et al. 2021, *CQGra*, **38**, 055010
 Chruslinska, M., & Nelemans, G. 2019, *MNRAS*, **488**, 5300
 Conroy, C., & Gunn, J. E. 2010, *ApJ*, **712**, 833
 Costa, G., Bressan, A., Mapelli, M., et al. 2021, *MNRAS*, **501**, 4514
 de Mink, S. E., & Belczynski, K. 2015, *ApJ*, **814**, 58
 de Mink, S. E., & Mandel, I. 2016, *MNRAS*, **460**, 3545
 Di Carlo, U. N., Mapelli, M., Giacobbo, N., et al. 2020, *MNRAS*, **498**, 495
 Dominik, M., Belczynski, K., Fryer, C., et al. 2012, *ApJ*, **759**, 52
 Edelman, B., Doctor, Z., Godfrey, J., & Farr, B. 2022, *ApJ*, **924**, 101
 El-Badry, K., Quataert, E., Weisz, D. R., Choksi, N., & Boylan-Kolchin, M. 2019, *MNRAS*, **482**, 4528
 Farmer, R., Renzo, M., de Mink, S. E., Fishbach, M., & Justham, S. 2020, *ApJL*, **902**, L36
 Farrell, E., Groh, J. H., Hirschi, R., et al. 2021, *MNRAS*, **502**, L40
 Fields, C. E., Timmes, F. X., Farmer, R., et al. 2018, *ApJS*, **234**, 19
 Fishbach, M., Zoheyr, D., Callister, T., et al. 2021, *ApJ*, **912**, 98
 Ford, K. E. S., & McKernan, B. 2021, arXiv:2109.03212
 Fragione, G., & Banerjee, S. 2020, *ApJL*, **901**, L16
 Fragione, G., Kocsis, B., Rasio, F. A., & Silk, J. 2022, *ApJ*, **927**, 231
 Fryer, C. L., Belczynski, K., Wiktorowicz, G., et al. 2012, *ApJ*, **749**, 91
 Fuller, J., & Ma, L. 2019, *ApJL*, **881**, L1
 Gaburov, E., Lombardi, J. C., & Portegies Zwart, S. 2008, *MNRAS*, **383**, L5
 Gallegos-Garcia, M., Berry, C. P. L., Marchant, P., & Kalogera, V. 2021, *ApJ*, **922**, 110
 García, F., Simaz Bunzel, A., Chaty, S., Porter, E., & Chassande-Mottin, E. 2021, *A&A*, **649**, A114
 Gerosa, D., & Kesden, M. 2016, PRECESSION: Python toolbox for dynamics of spinning black-hole binaries, Astrophysics Source Code Library, ascl:1611.004
 Gessner, A., & Janka, H.-T. 2018, *ApJ*, **865**, 61
 Giacobbo, N., & Mapelli, M. 2018, *MNRAS*, **480**, 2011
 Heggie, D., & Hut, P. 2003, *CQGra*, **20**, 4504
 Hénon, M. 1971, *Ap&SS*, **13**, 284

- Hénon, M. H. 1971, *Ap&SS*, **14**, 151
- Hobbs, G., Lorimer, D. R., Lyne, A. G., & Kramer, M. 2005, *MNRAS*, **360**, 974
- Hurley, J. R., Pols, O. R., & Tout, C. A. 2000, *MNRAS*, **315**, 543
- Hurley, J. R., Tout, C. A., & Pols, O. R. 2002, *MNRAS*, **329**, 897
- Lombardi, J. C., Warren, J., Rasio, J. S., et al. 2002, *ApJ*, **568**, 939
- Joshi, K. J., Rasio, F. A., & Portegies Zwart, S. P. 2000, *ApJ*, **540**, 969
- King, A. R., Davies, M. B., Ward, M. J., Fabbiano, G., & Elvis, M. 2001, *ApJL*, **552**, L109
- Kinugawa, T., Nakamura, T., & Nakano, H. 2021, *MNRAS*, **501**, L49
- Klencki, J., Moe, M., Gladysz, W., et al. 2018, *A&A*, **619**, A77
- Klencki, J., Nelemans, G., Istrate, A. G., & Chruslinska, M. 2021, *A&A*, **645**, A54
- Kremer, K., Spera, M., Becker, D., et al. 2020, *ApJ*, **903**, 45
- Kroupa, P. 2001, *MNRAS*, **322**, 231
- Leung, S.-C., Nomoto, K., & Blinnikov, S. 2019, *ApJ*, **887**, 72
- Lipunov, V. M., Postnov, K. A., & Prokhorov, M. E. 1997, *AstL*, **23**, 492
- MacLeod, M., Antoni, A., Murguia-Berthier, A., Macias, P., & Ramirez-Ruiz, E. 2017, *ApJ*, **838**, 56
- Madau, P., & Fragos, T. 2017, *ApJ*, **840**, 39
- Mandel, I., & Broekgaarden, F. S. 2022, *LRR*, **25**, 1
- Mandel, I., & de Mink, S. E. 2016, *MNRAS*, **458**, 2634
- Mapelli, M. 2016, *MNRAS*, **459**, 3432
- Mapelli, M., Dall'Amico, M., Bouffanais, Y., et al. 2021, *MNRAS*, **505**, 339
- Marchant, P., Langer, N., Podsiadlowski, P., Tauris, T. M., & Moriya, T. J. 2016, *A&A*, **588**, A50
- Mikkola, S., & Merritt, D. 2008, *AJ*, **135**, 2398
- Mikkola, S., & Tanikawa, K. 1999, *MNRAS*, **310**, 745
- Moe, M., & Di Stefano, R. 2017, *ApJS*, **230**, 15
- Mondal, S., Belczyński, K., Wiktorowicz, G., Lasota, J.-P., & King, A. R. 2020, *MNRAS*, **491**, 2747
- Neijssel, C. J., Vigna-Gomez, A., Stevenson, S., et al. 2019, *MNRAS*, **490**, 3740
- Nitadori, K., & Aarseth, S. J. 2012, *MNRAS*, **424**, 545
- O'Connor, E., & Ott, C. D. 2011, *ApJ*, **730**, 70
- Olejak, A., & Belczynski, K. 2021, *ApJL*, **921**, L2
- Olejak, A., Belczynski, K., & Ivanova, N. 2021, *A&A*, **651**, A100
- Olejak, A., Fryer, C. L., Belczynski, K., & Baibhav, V. 2022, arXiv:2204.09061
- Pattabiraman, B., Umbreit, S., Liao, W. K., et al. 2013, *ApJS*, **204**, 16
- Pavlovskii, K., Ivanova, N., Belczynski, K., & Van, K. X. 2017, *MNRAS*, **465**, 2092
- Peters, P. C. 1964, *PhRv*, **136**, 1224
- Podsiadlowski, P., Langer, N., Poelarends, A. J. T., et al. 2004, *ApJ*, **612**, 1044
- Podsiadlowski, P., Rappaport, S., & Han, Z. 2003, *MNRAS*, **341**, 385
- Portegies Zwart, S. F., & McMillan, S. L. W. 2000, *ApJL*, **528**, L17
- Portegies Zwart, S. F., McMillan, S. L. W., & Gieles, M. 2010, *ARA&A*, **48**, 431
- Qin, Y., Fragos, T., Meynet, G., et al. 2018, *A&A*, **616**, A28
- Rastello, S., Amaro-Seoane, P., Arca-Sedda, M., et al. 2019, *MNRAS*, **483**, 1233
- Rastello, S., Mapelli, M., Di Carlo, U. N., et al. 2021, *MNRAS*, **507**, 3612
- Rodriguez, C. L., Amaro-Seoane, P., Chatterjee, S., et al. 2018a, *PhRvD*, **98**, 123005
- Rodriguez, C. L., Amaro-Seoane, P., Chatterjee, S., & Rasio, F. A. 2018b, *PhRvL*, **120**, 151101
- Rodriguez, C. L., Chatterjee, S., & Rasio, F. A. 2016a, *PhRvD*, **93**, 084029
- Rodriguez, C. L., Haster, C.-J., Chatterjee, S., Kalogera, V., & Rasio, F. A. 2016b, *ApJL*, **824**, L8
- Rodriguez, C. L., & Loeb, A. 2018, *ApJL*, **866**, L5
- Rodriguez, C. L., Zevin, M., Amaro-Seoane, P., et al. 2019, *PhRvD*, **100**, 043027
- Roulet, J., Chia, H. S., Olsen, S., et al. 2021, *PhRvD*, **104**, 083010
- Safarzadeh, M., Hamers, A. S., Loeb, A., & Berger, E. 2020, *ApJL*, **888**, L3
- Samsing, J., Bartos, I., D'Orazio, D. J., et al. 2020, arXiv:2010.09765
- Sana, H., & Evans, C. J. 2011, in Proc. IAU Symp. 272, Active OB Stars: Structure, Evolution, Mass Loss, and Critical Limits, ed. C. Neiner et al. (Cambridge: Cambridge University Press), 474
- Sana, H., de Koter, A., de Mink, S. E., et al. 2013, *A&A*, **550**, A107
- Sana, H., de Mink, S. E., de Koter, A., et al. 2012, *Sci*, **337**, 444
- Santoliquido, F., Mapelli, M., Giacobbo, N., Bouffanais, Y., & Artale, M. C. 2021, *MNRAS*, **502**, 4877
- Schneider, A. S., Roberts, L. F., Ott, C. D., & O'Connor, E. 2019, *PhRvC*, **100**, 055802
- Sharda, P., Krumholz, M. R., Wisnioski, E., et al. 2021, *MNRAS*, **504**, 53
- Spera, M., Mapelli, M., Giacobbo, N., et al. 2019, *MNRAS*, **485**, 889
- Spitzer, L. 1987, Dynamical Evolution of Globular Clusters (Princeton, NJ: Princeton Univ. Press), 191, p
- Stevenson, S., Sampson, M., Powell, J., et al. 2019, *ApJ*, **882**, 121
- The LIGO Scientific Collaboration 2021a, arXiv:2111.03606
- The LIGO Scientific Collaboration 2021b, *ApJL*, **913**, L7, The LIGO Scientific Collaboration
- The LIGO Scientific Collaboration 2021c, arXiv:2111.03634
- Timmes, F. X., Woosley, S. E., & Weaver, T. A. 1996, *ApJ*, **457**, 834
- Tiwari, V. 2022, *ApJ*, **928**, 155
- Tiwari, V., & Fairhurst, S. 2021, *ApJL*, **913**, L19
- van den Heuvel, E. P. J., Portegies Zwart, S. F., & de Mink, S. E. 2017, *MNRAS*, **471**, 4256
- van Son, L. A. C., de Mink, S. E., Callister, T., et al. 2022, *ApJ*, **931**, 17
- Vink, J. S., & de Koter, A. 2005, *A&A*, **442**, 587
- Vink, J. S., de Koter, A., & Lamers, H. J. G. L. M. 2001, *A&A*, **369**, 574
- Voss, R., & Tauris, T. M. 2003, *MNRAS*, **342**, 1169
- Webbink, R. F. 1984, *ApJ*, **277**, 355
- Zampieri, L., & Roberts, T. P. 2009, *MNRAS*, **400**, 677
- Zevin, M., Bavera, S. S., Berry, C. P. L., et al. 2021, *ApJ*, **910**, 152
- Zevin, M., Spera, M., Berry, C. P. L., & Kalogera, V. 2020, *ApJL*, **899**, L1
- Zhang, Q. S. 2013, *ApJS*, **205**, 18